separations

MDPI

Article

Valorization of Phosphate Tailings into Ca-Mg-Al Layered Double Hydroxides for Phosphate Adsorption from Wastewater

Zhe Wang [1,2], Hongquan Jing [1,2], Bingbing Liu [2], Yixuan Zhang [1], Jiangli Li [1] and Cuihong Hou [2,*]

[1] National Engineering and Technology Research Center for Development & Utilization of Phosphate Re-Sources, Kunming 650000, China; 15378706921@163.com (Z.W.); jhqzzu@126.com (H.J.); 15887093384@163.com (J.L.)
[2] School of Chemical Engineering, Zhengzhou University, Zhengzhou 450001, China; liubingbing@zzu.edu.cn
* Correspondence: hch92@zzu.edu.cn

Abstract

Phosphate tailings (PTs), a solid waste generated from phosphate flotation, are a low-grade phosphate resource rich in quartz and dolomite. Their long-term accumulation leads to both resource loss and environmental risks, making valorization increasingly important for the sustainable development of the phosphorus chemical industry. In this study, calcareous–magnesian PTs were used as raw materials, and selective hydrothermal leaching with weakly acidic $AlCl_3$ solution was employed to separate the dolomite phase and directly construct a Ca-Mg-Al precursor solution for layered double hydroxides (LDHs). The LDHs were subsequently synthesized by co-precipitation and evaluated for phosphate removal from wastewater. The results showed that the precipitation pH markedly affected the phase composition and platelet morphology of the LDHs, while appropriate aging conditions further improved their adsorption performance. Under the optimal conditions of pH 12, aging at 40 °C for 2 h, the obtained LDHs exhibited the best phosphate uptake. Adsorption kinetics followed the pseudo-second-order model, and the maximum adsorption capacity calculated from the Langmuir model reached 38.61 mg-P/g. Characterization by XRD, FTIR, TG-DTA, point of zero charge, and XPS indicated that phosphate removal was dominated by surface complexation, accompanied by anion exchange, ionic precipitation, and electrostatic attraction.

Keywords: phosphate tailings; Ca-Mg-Al layered double hydroxides; selective leaching; phosphate adsorption; wastewater treatment

Check for updates

Academic Editor: Dimosthenis Giokas

Received: 29 May 2026
Revised: 19 June 2026
Accepted: 23 June 2026
Published: 25 June 2026

Copyright: © 2026 by the authors. Licensee MDPI, Basel, Switzerland. This article is an open access article distributed under the terms and conditions of the Creative Commons Attribution (CC BY) license.

1. Introduction

Excessive phosphate in water bodies is a major cause of eutrophication. The migration and transformation of phosphorus between lake water and sediments continuously affect water nutrient levels and algal growth processes [1]. Under hypoxic or anaerobic conditions, endogenous phosphorus release from sediments can be significantly intensified, further exacerbating the risk of lake eutrophication [2]. Recent studies have demonstrated that controlling sediment phosphorus release and enhancing phosphorus immobilization capacity in eutrophic lakes are critical strategies for mitigating internal phosphorus loading [3]. Among various phosphorus removal technologies, adsorption has become a research focus in phosphorus removal and recovery owing to its operational simplicity, high efficiency, relatively low cost, and broad applicability [4]. Nevertheless, the practical application of adsorbents remains constrained by factors such as adsorption capacity, selectivity, regenerability, and preparation cost [5]. Consequently, developing adsorbents that are derived

from abundant and inexpensive sources while possessing stable phosphate immobilization capacity is of great significance for both aquatic phosphorus pollution control and phosphorus resource recycling [6,7].

Phosphate rock is a vital raw material for phosphate fertilizer production, phosphorus-based chemical industries, and emerging energy materials. Its mining and beneficiation inevitably generate large quantities of Phosphate tailings (PTs). Approximately 0.44 tons of tailings are produced per ton of phosphate concentrate, and China generates nearly 10 million tons of PTs annually, with an overall utilization rate of only about 18% [8]. As high-grade phosphate ores are preferentially exploited, the proportion of tailings generated continues to increase, rendering their resource utilization a critical bottleneck constraining the green development of the phosphorus chemical industry. PTs typically comprise dolomite, calcite, quartz, fluorapatite, and minor iron and aluminum-bearing minerals. Prolonged stockpiling not only occupies extensive land resources but may also trigger fugitive dust emissions, soil and water contamination, tailings dam failure risks, and potential ecological hazards [9]. Currently, the comprehensive utilization of PTs mainly encompasses construction material preparation, backfilling, fertilizer production, and valuable element recovery [10,11]. Although these approaches can partially consume tailings, some pathways offer limited added value and fall short in the targeted transformation of valuable components such as Ca, Mg, and residual P in the tailings. Therefore, exploring efficient separation and functional utilization pathways for valuable components in PTs is of considerable importance for achieving their volume reduction, resource recovery, and high-value valorization [12].

Layered double hydroxides (LDHs) are a class of two-dimensional layered materials with hydrotalcite-like structures, generally represented by the formula $[M^{2+}_{1-x}M^{3+}_{x}(OH)_2]^{x+}(A^{n-})_{x/n}\cdot yH_2O$, where M^{2+} and M^{3+} denote divalent and trivalent metal cations (commonly Ca^{2+}, Mg^{2+}, Fe^{3+}, and Al^{3+}), and A^{n-} represents interlayer exchangeable anions [13]. Owing to their excellent anion exchange capacity, high specific surface area, favorable thermal stability, and tunable performance achievable through the regulation of metal cation composition and interlayer anion species, LDHs have demonstrated promising application prospects for the removal of phosphate and other oxyanion pollutants [14–16]. In recent years, increasing research efforts have been devoted to preparing LDH-based adsorbents from industrial solid wastes such as blast furnace slag, fly ash, and aluminum dross, which not only reduces material preparation costs but also opens new avenues for solid waste valorization [15–17]. Notably, certain PTs are enriched in Ca and Mg, presenting inherent raw material characteristics favorable for synthesizing Ca-Mg-based LDHs.

In this study, based on the mineralogical composition of calcareous–magnesian PTs, the weakly acidic conditions generated by $AlCl_3$ hydrolysis were exploited to achieve highly selective leaching of the dolomite phase while suppressing the dissolution of fluorapatite and quartz, thereby simultaneously establishing a Ca-Mg-Al precursor solution system. The leachate was subsequently converted into Ca-Mg-Al LDHs via co-precipitation, and the effects of synthesis parameters on the LDH structure and phosphate removal performance were systematically investigated to identify optimal preparation conditions. Furthermore, the phosphate adsorption performance and removal mechanisms of the resulting LDHs were comprehensively evaluated through adsorption kinetics, isotherm modeling, and multiple characterization techniques, aiming to provide theoretical insights and technical references for the high-value utilization of PTs and the treatment of phosphorus-laden wastewater.

2. Materials and Methods

2.1. Materials

2.1.1. Chemical Reagents

PTs used in this study were collected from Yunnan, China. Before use, the PTs were dried at 110 °C for 5 h to remove surface moisture. Anhydrous aluminum chloride ($AlCl_3$) was purchased from Shanghai Macklin Biochemical Co., Ltd. (Shanghai, China). The phosphorus standard solution was obtained from the National Center of Analysis and Testing for Nonferrous Metals and Electronic Materials. Hydrochloric acid (HCl) was supplied by Xilong Scientific Co., Ltd. (Shantou, China), and sodium hydroxide (NaOH) was purchased from Rhawn Reagent (Shanghai, China). All chemicals used were of analytical grade, and deionized water was used throughout the experiments. PTs used in this study were collected from a phosphate mining enterprise in Yunnan, China. Before use, the PTs were dried at 110 °C for 5 h to remove surface moisture. Anhydrous aluminum chloride ($AlCl_3$) and sodium hydroxide (NaOH) were purchased from Rhawn Reagent. The phosphorus standard solution was obtained from the National Center of Analysis and Testing for Nonferrous Metals and Electronic Materials (Beijing, China). Hydrochloric acid (HCl) was supplied by Xilong Scientific Co., Ltd. All chemicals used were of analytical grade, and deionized water was used throughout the experiments.

2.1.2. Mineralogical Analysis of PTs

The mineralogical characteristics of the PTs are shown in Figure 1. Based on the X-ray diffraction (XRD), X-ray fluorescence spectroscopy (XRF), and scanning electron microscopy coupled with energy-dispersive spectroscopy (SEM-EDS) mapping results, the PTs were mainly composed of dolomite ($CaMg(CO_3)_2$), fluorapatite ($Ca_5(PO_4)_3F$), and quartz (SiO_2). The XRD pattern indicated that dolomite was the dominant crystalline phase in the PTs, whereas fluorapatite and quartz were present in relatively small amounts. The XRF results (Table 1) showed that the contents of CaO, MgO, SiO_2, P_2O_5, and F in the PTs were 36.96%, 11.38%, 5.06%, 4.52%, and 0.37%, respectively, with a loss on ignition (LOI) of 36.90%. Without considering the influence of trace elements, the total mass fraction of $CaCO_3$ and $MgCO_3$ in the PTs was calculated to be 79.47 wt% based on the mass conservation relationship between the total oxide content of the phosphate tailings and the oxide content of each mineral phase [18].

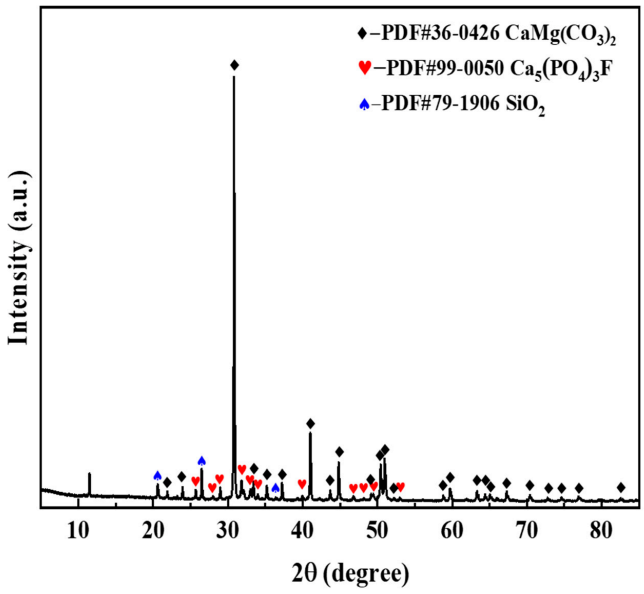


Figure 1. XRD pattern of Phosphate tailings (PTs).

Table 1. Chemical composition of Phosphate tailings (PTs).

Composition	CaO	MgO	SiO_2	P_2O_5	SO_3	Fe_2O_3	Al_2O_3	F	LOI [1] (%)
wt.%	36.96	11.38	5.06	4.52	2.49	0.92	0.73	0.37	36.90

[1] LOI: loss on ignition. The LOI value was tested at 950 °C.

The morphology and elemental distribution of the PTs are shown in Figure 2. As shown in Figure 2a–c, the PTs particles exhibited irregular fragmental morphologies, with fine and coarse particles cemented together. The EDS mapping results showed that the larger mineral particles in Figure 2d,e were mainly dolomite. Mg was primarily enriched in dolomite, P and F were mainly associated with fluorapatite, and Si was concentrated in quartz, while Ca was distributed in both dolomite and fluorapatite. These results indicate that the liberation degree of apatite was relatively low, and apatite was commonly encapsulated by or intergrown with dolomite and quartz [12].

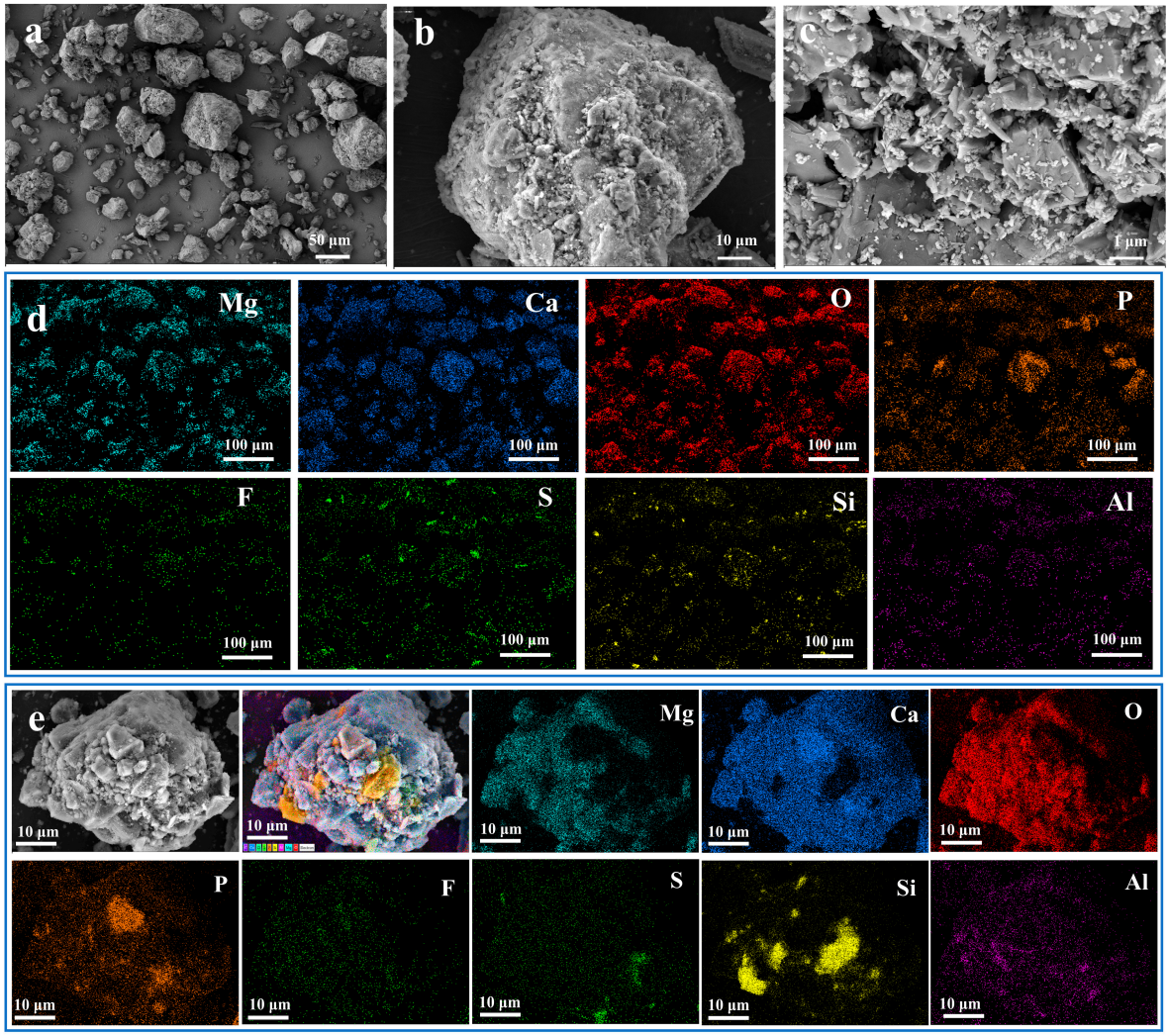


Figure 2. SEM (**a**–**c**) and EDS (**d**,**e**) analysis of PTs.

2.2. Synthesis of Ca-Mg-Al LDHs from PTs

The PTs used in this study were collected from a phosphate mining enterprise in Yunnan Province, China. Prior to synthesis, the PTs were ball-milled to a particle size of less than 200 mesh. Subsequently, LDHs were prepared via a hydrothermal-assisted leaching-coprecipitation method [19]. Specifically, 2.5000 g of PTs was weighed and placed

in a Teflon-lined stainless-steel autoclave (Jiangsu Taifulong Anticorrosive Equipment Co., Ltd., Taixing, China), followed by the addition of an $AlCl_3$ solution with a specified concentration. The mixture was then subjected to hydrothermal treatment at 200 °C for 6 h. After the reaction, the autoclave was naturally cooled to room temperature, and the leachate containing Ca, Mg, and Al metal ions was obtained by solid–liquid separation.

Subsequently, 2 mol/L NaOH solution was added dropwise to the leachate under continuous stirring to adjust the system pH to the predetermined value. The resulting suspension was further aged at the specified temperature for a certain period to promote the formation and structural development of the LDH crystalline phase. After aging, the product was filtered and repeatedly washed with deionized water to remove residual ions. Finally, the obtained solid was dried overnight at 80 °C and ground into powder for subsequent phosphate adsorption tests and material characterization. The preparation procedure of the LDHs is illustrated in Figure 3, and the detailed synthesis conditions are listed in Table 2.

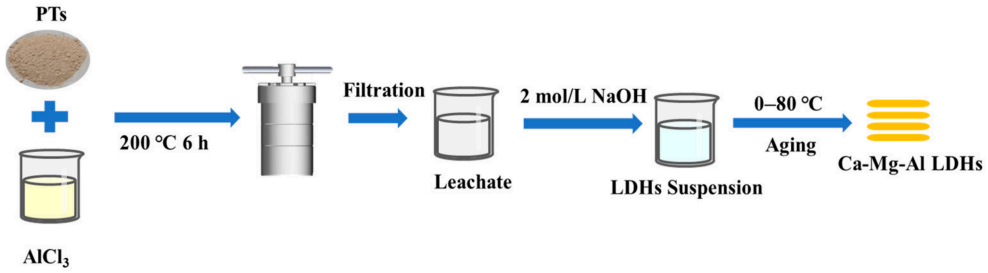


Figure 3. Schematic illustration of the synthesis process of LDHs.

Table 2. Operational parameters for LDHs synthesis.

Conditions	pH	Temperature (°C)	Aging Time (h)
Effect of pH	9, 10, 11, 12, 13	40	2
Effect of temperature	12	0, 20, 40, 60, 80	2
Effect of aging time	12	40	0, 1, 2, 4, 8

2.3. Adsorption Experiments

Phosphate adsorption experiments were conducted at room temperature with a stirring rate of 500 r/min. To evaluate the phosphate adsorption behavior of Ca-Mg-Al LDHs, adsorption kinetic and isothermal adsorption experiments were carried out separately, and the phosphate immobilization mechanism was further analyzed in combination with subsequent characterization results.

For the kinetic experiments, 0.0500 g of the synthesized LDHs was added to 40 mL of phosphate solution with an initial phosphorus concentration of 50 mg/L. Samples were collected at predetermined time intervals of 2, 10, 20, 30, 60, 90, 120, 150, 180, 210, and 240 min to investigate the variation in adsorption capacity with contact time.

For the isothermal adsorption experiments, 0.1000 g of the synthesized LDHs was added to 40 mL of phosphate solutions with initial phosphorus concentrations of 2, 5, 10, 20, 40, 60, 80, 100, 150, and 200 mg/L until adsorption equilibrium was reached, in order to evaluate the equilibrium adsorption performance of the material under different initial concentration conditions.

After the reaction, the suspension was filtered through a 0.45 μm membrane, and the residual phosphorus concentration in the filtrate was determined using a UV-vis spectrophotometer (NB-T9, Yipu Instrument Manufacturing Co., Ltd., Shanghai, China).

The phosphorus adsorption capacity and removal efficiency of the LDHs were calculated according to Equation (1) and Equation (2), respectively:

$$q_e = \frac{(C_0 - C_e) \times V}{m} \quad (1)$$

$$R = \frac{C_0 - C_e}{C_0} \times 100\% \quad (2)$$

where C_0 and C_e (mg/L) are the initial and equilibrium concentrations of phosphorus in the solution, respectively; m (g) is the mass of the adsorbent; and V (L) is the volume of the solution.

2.4. Characterization and Analytical Methods

The chemical composition of the PTs was analyzed by X-ray fluorescence spectroscopy (XRF, XRF-1800, Shimadzu Corporation, Kyoto, Japan). The elemental contents of the LDHs were determined using an inductively coupled plasma optical emission spectrometer (ICP-OES, ICPOES-9820, Shimadzu Corporation, Kyoto, Japan). The phase structure of the products was characterized by X-ray diffraction (XRD, SmartLab SE, Rigaku Corporation, Tokyo, Japan). The morphology and elemental distribution of the samples were observed using scanning electron microscopy coupled with energy-dispersive spectroscopy (SEM-EDS, Sigma 300, Carl Zeiss Microscopy GmbH, Jena, Germany). The surface functional groups of the samples were determined by Fourier transform infrared spectroscopy (FTIR; Nicolet iS20, Thermo Fisher Scientific Inc., Waltham, MA, USA) in the wavenumber range of 4000–400 cm^{-1}. The point of zero charge (pH_{PZC}) of the LDHs was determined using the pH drift method with a pH meter (PHS-3C, Shanghai INESA Scientific Instrument Co., Ltd., Shanghai, China). Thermogravimetric analysis (TGA) and differential thermal analysis (DTA) were performed using a simultaneous thermal analyzer (STA 449 F5, NETZSCH-Gerätebau GmbH, Selb, Germany) to evaluate the thermal stability at a heating rate of 5 °C/min under a nitrogen atmosphere. The surface elemental composition and chemical states of the samples before and after phosphate adsorption were analyzed by X-ray photoelectron spectroscopy (XPS, K-Alpha, Thermo Fisher Scientific Inc., Waltham, MA, USA), and the binding energies were calibrated using the C 1s peak at 284.8 eV.

3. Results and Discussion

3.1. Synthesis Process Optimization of Ca-Mg-Al LDHs

3.1.1. Characteristics of the Ca-Mg-Al LDHs Precursor Solution

Based on preliminary experimental investigations, the optimal hydrothermal leaching conditions were determined as follows: hydrothermal temperature of 200 °C, reaction time of 6 h, $AlCl_3$ solution concentration of 0.35 mol/L, and liquid-to-solid ratio of 24 mL/g. Under these conditions, the dolomite phase in the PTs was efficiently decomposed while the fluorapatite phase exhibited minimal dissolution, yielding a leachate enriched in Ca, Mg, and Al with a low P content, which served as the precursor solution for Ca-Mg-Al LDHs synthesis. The elemental concentrations in the precursor solution and the leaching rates of Ca, Mg, and P are summarized in Table 3. The results indicated that the leaching rates of Ca, Mg, and P were 77.87%, 99.69%, and 7.53%, respectively, with 34% of Al remaining in the liquid phase. The solution pH was 2.84, confirming an acidic environment suitable for subsequent co-precipitation of LDHs.

Table 3. Elemental contents of the precursor solution for Ca-Mg-Al LDH synthesis.

Composition	Ca	Mg	Al	P
Concentration (mg/L)	8915	4385	3298	68
Leaching efficiency (%)	77.87	99.69	34.48	7.53

3.1.2. Effect of Synthesis pH

The pH of the reaction system is a critical factor governing LDHs synthesis. This section first examines the influence of solution pH on the crystal structure, elemental composition, and phosphate removal performance of Ca-Mg-Al LDHs. Previous studies by Guo and Bader Bouzar et al. [20,21] have demonstrated that under relatively low pH conditions, Mg^{2+} precipitates preferentially over Ca^{2+}, while Ca^{2+} remains in the dissolved state and Al^{3+} partially substitutes for Mg^{2+} in the brucite-like layers through isomorphous replacement, resulting in the predominant formation of Mg-Al LDHs. Ca^{2+} commences precipitation only when the pH exceeds 10. Figure 4a presents the XRD patterns of samples synthesized at different pH values. At pH = 9–11, symmetric characteristic diffraction peaks appeared at approximately 2θ = 11° and 22°, accompanied by broad and weak reflections near 38°, 60°, and 61°, corresponding to the (003), (006), (015), (110), and (113) planes of LDHs, respectively. These patterns exhibit typical LDH diffraction features, confirming the successful synthesis of LDH materials. However, detailed XRD analysis revealed that the products synthesized within this pH range more closely matched the structural characteristics of $Mg_{0.833}Al_{0.167}(OH)_2(CO_3)_{0.833}(H_2O)_{0.75}$. Table 4 summarizes the major elemental compositions of LDHs synthesized at different pH values. With increasing solution pH, the Ca content in the LDHs samples progressively increased. At $9 \leq pH \leq 11$, the Ca content remained below 1%, and the predominant phase was identified as Mg-Al-CO_3 hydrotalcite, indicating that Ca^{2+} could hardly participate in LDHs formation under these conditions. When the pH was elevated to 12 and 13, the Ca content in the samples increased substantially to 6.13% and 11.67%, respectively, confirming that a higher pH environment facilitates Ca^{2+} precipitation and its incorporation into the LDH layers. XRD analysis further indicated that at $pH \geq 12$, the primary phases consisted of a mixture of Ca-Al-CO_3/Cl and Mg-Al-CO_3/Cl hydrotalcite-like compounds. Nevertheless, as the pH continued to rise, a minor amount of $CaCO_3$ impurity was detected in the dried LDH samples prepared at excessively high pH. An overly alkaline environment promotes the preferential precipitation of Ca^{2+} as $Ca(OH)_2$, which is unfavorable for the effective incorporation of Ca into the LDH layer structure, while also complicating sample washing and resulting in wasteful consumption of Ca^{2+}. Meanwhile, as shown in Figure 4b, the sample synthesized at pH = 12 exhibited the highest phosphate adsorption capacity and removal efficiency, reaching 19.59 mg-P/g and 98.47%, respectively. Based on these findings, the optimal synthesis pH was determined to be 12. It is generally recognized that for phase-pure LDHs, the molar ratio of $M^{3+}/(M^{3+} + M^{2+})$, denoted as the x value in the general formula, typically falls within the range of 0.17–0.33. The Ca-Mg-Al LDHs synthesized under the optimal conditions exhibited an x value of 0.29, which satisfies this criterion and ensures the formation of coexisting Ca-Al and Mg-Al LDH phases.

The micromorphologies of samples synthesized at different pH values are shown in Figure 5a–f. It can be clearly observed that at pH = 9, 10, 11, and 13, the LDHs samples exhibited severe agglomeration. In contrast, at pH = 12, the LDH nanosheets displayed well-defined lamellar structures with discernible interlayer voids, an interlocking and stacking arrangement, and clearly delineated edges without apparent agglomeration [22], suggesting that this pH condition is conducive to the nucleation and growth of LDH nanosheets. EDS elemental mapping analysis (Figure 5i–n) confirmed the uniform distribution of Mg, Al,

Ca, and Cl throughout the sample. A trace amount of P was also detected within the LDHs structure, exhibiting a relatively homogeneous distribution.

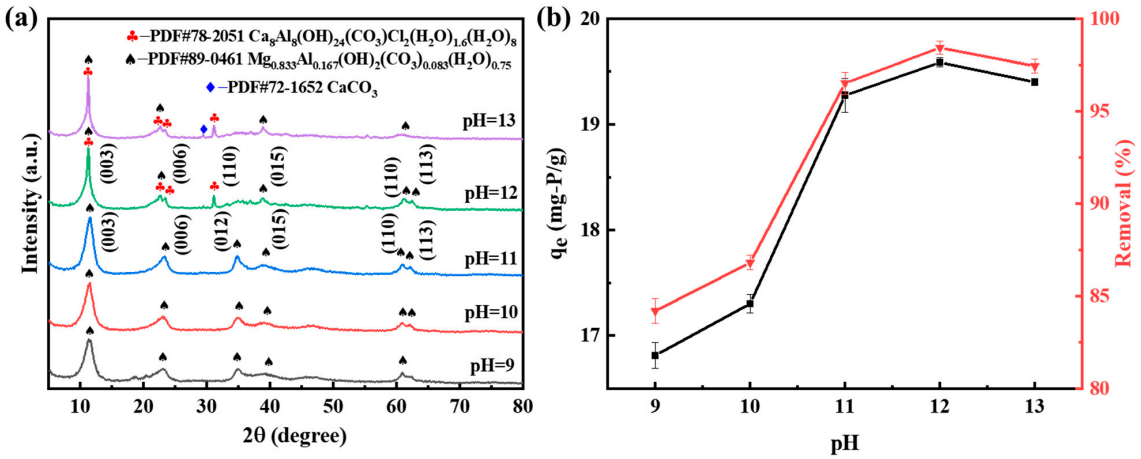


Figure 4. (**a**) XRD patterns and (**b**) phosphate removal efficiency of Ca-Mg-Al LDHs synthesized at different pH values.

Table 4. Elemental composition of LDHs synthesized at different pH values.

pH	Elemental Composition (%)				x
	Ca	Mg	Al	P	
9	0.28	18.72	13.87	0.37	0.40
10	0.79	21.80	11.93	0.33	0.33
11	0.86	20.98	10.91	0.30	0.31
12	6.13	21.10	11.25	0.35	0.29
13	11.67	16.65	9.57	0.22	0.27

3.1.3. Effect of Aging Temperature

The influence of aging temperature (0–80 °C) on the crystallographic properties and phosphate removal performance of LDHs was investigated. Figure 6a presents the XRD patterns of samples crystallized at different aging temperatures, while Figure 6b displays the corresponding phosphate adsorption capacities and removal efficiencies. At 0 °C and 20 °C, only the characteristic diffraction peaks of the Mg-Al LDH phase were observed, with no discernible reflections attributable to the Ca-Al LDH phase. In contrast, samples aged at 40, 60, and 80 °C exhibited well-resolved diffraction peaks indicative of the coexistence of both Ca-Al LDH and Mg-Al LDH phases. Notably, the diffraction peaks of samples prepared at 0 °C and 20 °C were relatively broad with low intensities, suggesting that these temperatures are insufficient to promote adequate crystallization of LDHs or the formation of the Ca-Al LDH phase, which corresponded to comparatively low phosphate adsorption capacities of approximately 14.40 and 15.97 mg-P/g, respectively. At 40 °C, the characteristic diffraction peaks became notably sharper and more intense, particularly the reflection near 2θ = 11° as well as those at approximately 22°, 23°, 31° and 38°, indicating that 40 °C represents the most favorable temperature for the synergistic formation of both Ca-Al and Mg-Al LDH phases. Consistent with this observation, the sample aged at 40 °C exhibited the highest phosphate removal performance, achieving an equilibrium adsorption capacity of 19.72 mg-P/g and a removal efficiency of 99.07%. When the aging temperature was further increased to 60 °C and 80 °C, the diffraction peaks remained well-defined; however, the adsorption capacity decreased slightly, suggesting that excessive crystallization may reduce the accessibility of active adsorption sites. Based on these findings, with all other synthesis parameters held constant, 40 °C was identified as the optimal aging temperature that achieves

an effective balance between the degree of crystallinity of Ca-Mg-Al LDHs and their phosphate removal performance.

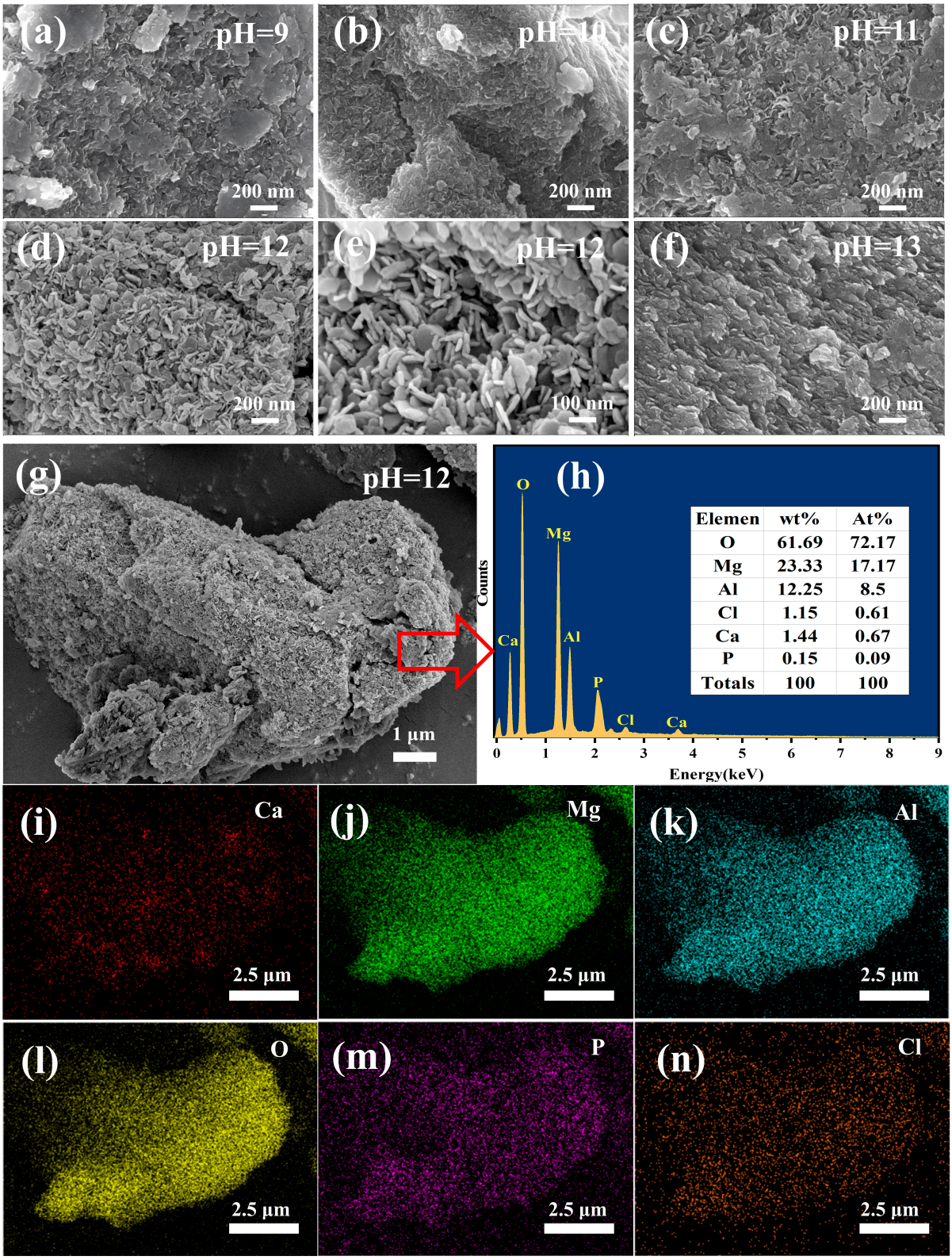


Figure 5. (**a**–**f**) SEM images of the samples prepared at pH 9–13, with panel (**e**) showing a higher-magnification image of the sample prepared at pH 12; (**g**–**n**) SEM-EDS results and elemental mappings of the sample prepared at pH 12, where (**g**) is the SEM image, (**h**) is the EDS spectrum, and (**i**–**n**) represent the mappings of Ca, Mg, Al, O, P, and Cl, respectively.

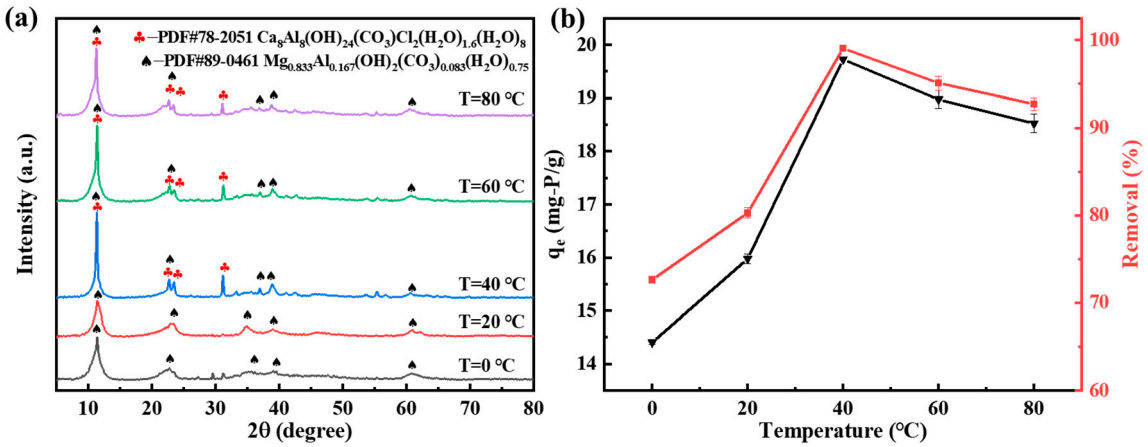


Figure 6. (**a**) XRD patterns and (**b**) phosphate removal performance of LDH samples synthesized at different aging temperatures.

3.1.4. Effect of Aging Time

During the synthesis of LDHs, the aging time simultaneously influences nucleation and crystal growth processes. As shown in Figure 7a, samples prepared under different aging durations (0, 1, 2, 4, and 8 h) all exhibited characteristic LDH diffraction peaks, indicating that a layered structure was formed under each condition. For the unaged sample and the sample aged for 1 h, the diffraction peaks were relatively broad with low intensities, and only the characteristic reflections of the Mg-Al LDH phase were identified. Upon extending the aging time to 2 h, characteristic peaks corresponding to both Ca-Al LDH and Mg-Al LDH phases appeared simultaneously, exhibiting well-defined, high-intensity, and sharp peak profiles, particularly the reflection near 2θ = 11° along with those at approximately 22°, 23°, 31° and 38°. This result demonstrates that an appropriate aging duration facilitates the formation and structural ordering of both Mg-Al LDH and Ca-Al LDH crystalline phases. When the aging time was further extended to 4 h, the intensity of the Ca-Al LDH characteristic peaks diminished and the full width at half maximum (FWHM) increased, with Mg-Al LDH becoming the dominant crystalline phase. This observation suggests that prolonged aging may lead to the degradation of the Ca-Al LDH ordered structure, reduced crystallinity, or localized structural rearrangement. After aging for 8 h, no characteristic peaks of Ca-Al LDH were detected; however, the formation of $CaCO_3$ was observed in the sample. The phosphate adsorption performance of samples prepared at different aging times is presented in Figure 7b. The adsorption capacity and removal efficiency reached their maximum values at an aging time of 2 h, corresponding to 19.58 mg-P/g and 98.13%, respectively. At aging times of 4 and 8 h, the adsorption performance declined slightly. Based on these results, 2 h was identified as the optimal aging time.

3.2. Adsorption Isotherms and Kinetics

Adsorption isotherms are mathematical models that describe the distribution of the adsorbate species among the liquid and adsorbent based on a set of assumptions that are mainly related to the heteroge-neity/homogeneity of adsorbents, the type of coverage and the possi-bility of interaction between the adsorbate species [23]. Langmuir (Equation (3)) and the Freundlich (Equation (4)) equations are commonly used to describe the adsorption equilibrium. The Langmuir model assumes monolayer adsorption on a homogeneous surface with no interactions between the adsorbed molecules; while the Freundlich model

is an empirical equation, which is often used to describe chemisorption on a heterogeneous surface [24].

$$q_e = \frac{q_m K_L C_e}{1 + K_L C_e} \tag{3}$$

$$q_e = K_F C_e^{\frac{1}{n}} \tag{4}$$

where q_e (mg g^{-1}) is the equilibrium adsorption amount at the equilibrium concentration of C_e (mg L^{-1}); q_m (mg g^{-1}) is the maximum capacity of the adsorbent; K_L (mg L^{-1}) is the Langmuir constant; K_F is the Freundlich constant; n is the Freundlich affinity coefficient.

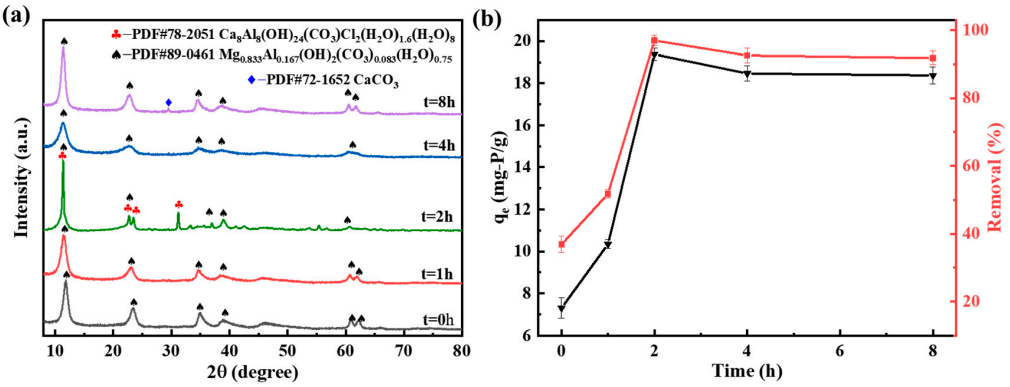


Figure 7. (**a**) The XRD patterns and (**b**) phosphate removal performance of LDH samples as a function of aging time.

As illustrated in Figure 8a, the equilibrium adsorption capacity of LDHs for phosphate gradually increases with increasing equilibrium phosphate concentration and subsequently approaches a plateau at higher concentration levels, indicating a characteristic saturation tendency. This behavior suggests that, within the low-concentration range, abundant accessible active sites are available on the LDHs surface, allowing phosphate to be rapidly captured. As the equilibrium concentration further increases, however, these active sites become progressively occupied, resulting in a diminished increase in adsorption capacity.

The fitting parameters obtained from the experimental data for the two models are presented in Table 5. Comparing the coefficients of determination (R^2) listed in Table 5, it can be concluded that the phosphate adsorption process fits better to the Langmuir model with R^2 = 0.9828.

Table 5. Fitting parameters of the adsorption isotherm models.

Sample	Langmuir			Freundlich		
	q_m (mg/g)	K_L (L/mg)	R^2	K_F	1/n	R^2
LDHs	38.61	0.2776	0.9828	11.5415	0.2863	0.9155

This result indicates that phosphate adsorption is generally closer to a monolayer adsorption process governed by a finite number of active sites [25]. The theoretical maximum adsorption capacity calculated from the Langmuir model is 38.61 mg-P/g, demonstrating the appreciable phosphate uptake capability of the Ca-Mg-Al LDHs. Meanwhile, the Freundlich constant of $1/n$ is 0.2863, which is lower than 1, indicating that the adsorption process is favorable. This value also suggests the presence of surface-site heterogeneity, which may be associated with the multi-metal composition, layered architecture, and surface defects of the Ca-Mg-Al LDHs [26]. Overall, phosphate adsorption by Ca-Mg-Al LDHs exhibits both the finite-site and saturation characteristics described by the Langmuir model, as well as a certain degree of surface heterogeneity. These results suggest that the

adsorption process is jointly influenced by active-site occupation, surface complexation, and anion exchange.

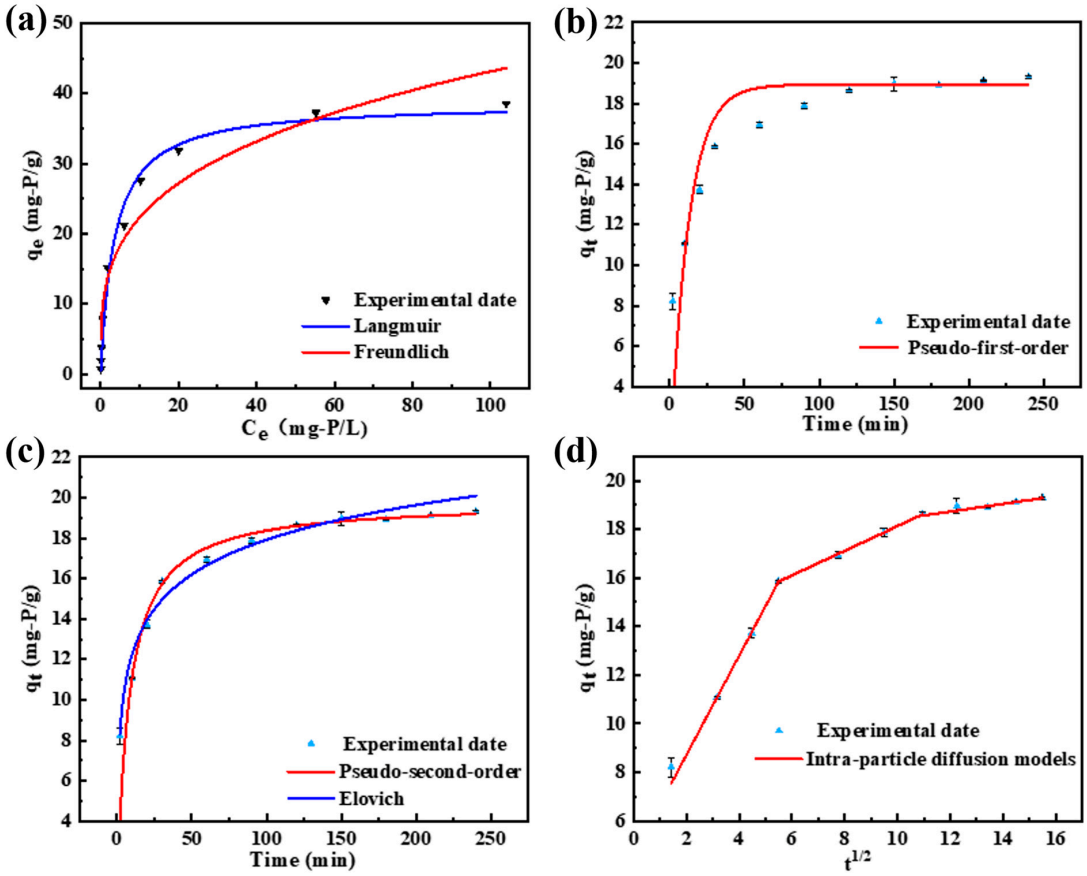


Figure 8. (**a**) Phosphate adsorption isotherms fitted by the Langmuir and Freundlich models; (**b**–**d**) adsorption kinetics fitted by the (**b**) pseudo-first-order, (**c**) pseudo-second-order, and (**d**) intraparticle diffusion models for phosphate removal by Ca-Mg-Al LDHs.

To identify the rate-controlling step of phosphate adsorption, the effect of contact time on phosphate removal by Ca-Mg-Al LDHs was investigated. As shown in Figure 8b,c, the phosphate adsorption capacity increased rapidly within the first 30 min, with more than 50% of phosphate removed during the initial 10 min, indicating the presence of abundant, readily available active sites on the material surface [27].

To identify the correct mechanism of phosphate adsorption by LDHs, four mathematical models were employed: pseudo-first-order (Equation (5)),pseudo-second-order (Equation (6)), Elovich (Equation (7)) and intraparticle diffusion (Equation (8)) models that are represented by the following equations [28–30]:

$$q_t = q_e\left(1 - e^{-k_1 t}\right) \quad (5)$$

$$q_t = \frac{k_2 t q_e^2}{1 + k_2 t q_e} \quad (6)$$

$$q_e = \frac{1}{\beta}(ln(\alpha\beta t + 1)) \quad (7)$$

$$q_t = k_d t^{0.5} + C \quad (8)$$

where q_t and q_e are the phosphate adsorption capacities at time t and at equilibrium, respectively (mg-P g^{-1}); k_1 (min^{-1}), k_2 (g mg^{-1} min^{-1}), and k_d (mg g^{-1} $min^{-0.5}$) are the

rate constants of the pseudo-first-order, pseudo-second-order, and intraparticle diffusion models, respectively; α is the initial adsorption rate (mg g^{-1});and β is the desorption constant (g mg^{-1}); and C is a constant in the intraparticle diffusion equation, corresponding to the thickness of the boundary layer.

As summarized in Table 6, the pseudo-second-order kinetic model provides a better fit to the experimental data, with a higher correlation coefficient (R^2 = 0.9917) than that of the pseudo-first-order model (R^2 = 0.9429)and the Elovich model (R^2 = 0.8955). This result indicates that phosphate adsorption onto Ca-Mg-Al LDHs follows pseudo-second-order kinetic behavior more closely. Accordingly, the adsorption rate is likely associated with the occupation of surface-active sites and interfacial chemical interactions, suggesting that phosphate removal may involve surface complexation, ligand exchange, and chemical immobilization mediated by metal sites. This finding is consistent with previous studies reporting that phosphate adsorption on LDH-based materials is commonly well described by the pseudo-second-order kinetic model [26,31].

In order to investigate whether any intra-particle diffusion is a rate-limiting factor in the adsorption process, the intraparticle diffusion model was taken into account. If the intraparticle diffusion is rate-limited, the plot of q_t vs. $t^{1/2}$ would be linear; the slope of the linearized plot characterizes the rate parameter of intra-particle diffusion, while the intercept is proportional to the thickness of the boundary layer [32]. As seen in Figure 8d, the plot is not linear over the entire time range and shows more than one linear portion, suggesting a multi-step process. Each step is identified by a change in the slope of the linear line, which is used to fit the experimental data. Thus three linear regions are identified: (a) the first region is attributed to the diffusion of phosphate through the solution to the external surface of the LDHs, (b) the second region describes the gradual adsorption stage in which the intraparticle diffusion is the rate limiting step, and (c) the third region is attributed to the final equilibrium stage where intraparticle diffusion starts to slow down due to low phosphate in the solution [33,34]. These results suggest that phosphate adsorption by Ca-Mg-Al LDHs is controlled by a combination of external film diffusion, intraparticle diffusion, and interfacial chemical interactions rather than by a single diffusion process.

Table 6. Fitting parameters of the adsorption kinetic models for phosphate adsorption by LDHs.

Model	Parameters		
Pseudo-first-order kinetic model		k_1	0.0812
		q_e (mg/g)	18.9223
		R^2	0.9429
Pseudo-second-order kinetic model		k_2	6.45×10^{-3}
		q_e (mg/g)	19.8080
		R^2	0.9917
Elovich		α	34.5328
		β	0.4042
		R^2	0.8955
Intra-particle diffusion model	Step1	k_3	2.0397
		C_3	4.6506
		R^2	0.9983
	Step2	k_4	0.5064
		C_4	13.0630
		R^2	0.9997
	Step3	k_5	0.1593
		C_5	16.8090
		R^2	0.9520

3.3. Phosphate Adsorption Mechanism

To elucidate the phosphate removal mechanism of Ca-Mg-Al LDHs, the crystal structure, functional groups, thermal stability, point of zero charge (pH_{PZC}), and surface chemical states before and after adsorption were comparatively analyzed, alongside solution pH evolution and phosphate speciation. The results are presented in Figures 9 and 10. The XRD patterns (Figure 9a) confirmed that characteristic diffraction peaks of the (003), (006), (012), (015), (110), and (113) planes were retained after phosphate adsorption with no appreciable peak shift or the full width at half maximum (FWHM) broadening, indicating that the layered structure remained intact without interlayer expansion [35]. The absence of new crystalline phases suggests that anion exchange was not the predominant mechanism and that phosphate removal occurred primarily through surface complexation [36]. FTIR analysis (Figure 9b) revealed that the CO_3^{2-} antisymmetric stretching band at 1360.20 cm^{-1} weakened and shifted slightly to 1363.10 cm^{-1} after adsorption, indicating partial displacement of carbonate by phosphate [37]. Two new peaks emerged at 1059.80 cm^{-1} and 952.80 cm^{-1}, assigned to P-O stretching and M-O-P bonding vibrations, respectively [37,38], providing direct spectroscopic evidence of inner-sphere complexation. The M-O and M-OH lattice vibrations below 800.00 cm^{-1} remained well preserved, corroborating structural stability. TG-DTA (Figure 9c) showed that the total weight loss decreased from 50.32% to 35.94% after adsorption across three stages: dehydration (50–220 °C: 15.54% → 10.99%), dehydroxylation (220–480 °C: 25.51%→ 18.73%), and interlayer anion decomposition (480–970 °C: 9.27% → 6.22%). The reduced weight loss in the first two stages reflects altered hydration and hydroxyl environments due to phosphate occupation, while the third-stage reduction is attributable to partial replacement of thermally decomposable Cl^-/CO_3^{2-} by phosphate. Notably, the endothermic peak positions remained essentially unchanged, confirming that phosphate modified the composition rather than the fundamental decomposition pathway of the LDHs framework. As shown in Figure 9g, Metal ion dissolution monitoring revealed that Ca^{2+} and Mg^{2+} concentrations increased rapidly during the initial adsorption stage before stabilizing (maximum < 4 mg/L), while Al^{3+} remained below 0.1 mg/L throughout, demonstrating that only limited surface dissolution occurred without compromising the layer framework integrity. As shown in Figure 9e, the solution pH increased progressively from 7.98 to 8.80, reaching equilibrium at approximately 300 min. This elevation reflects OH^- release from ligand exchange at M-OH sites. According to the phosphate speciation diagram (Figure 9f), HPO_4^{2-} is the predominant species within this pH range, establishing it as the primary adsorbate. The pH_{PZC} (Figure 9d) decreased from 9.70 to 8.50 after adsorption ($\Delta pH_{PZC} = -1.20$). Since the working pH (7.98) remained below pH_{PZC} (9.70), the surface maintained a net positive charge throughout, providing the electrostatic driving force for the HPO_4^{2-} approach. Critically, the substantial negative pH_{PZC} shift constitutes definitive evidence of inner-sphere complexation, as outer-sphere or purely electrostatic interactions cannot induce measurable pH_{PZC} displacement, and only specific adsorption through covalent M-O-P bonding can increase the net surface negative charge density sufficiently to produce such a shift.

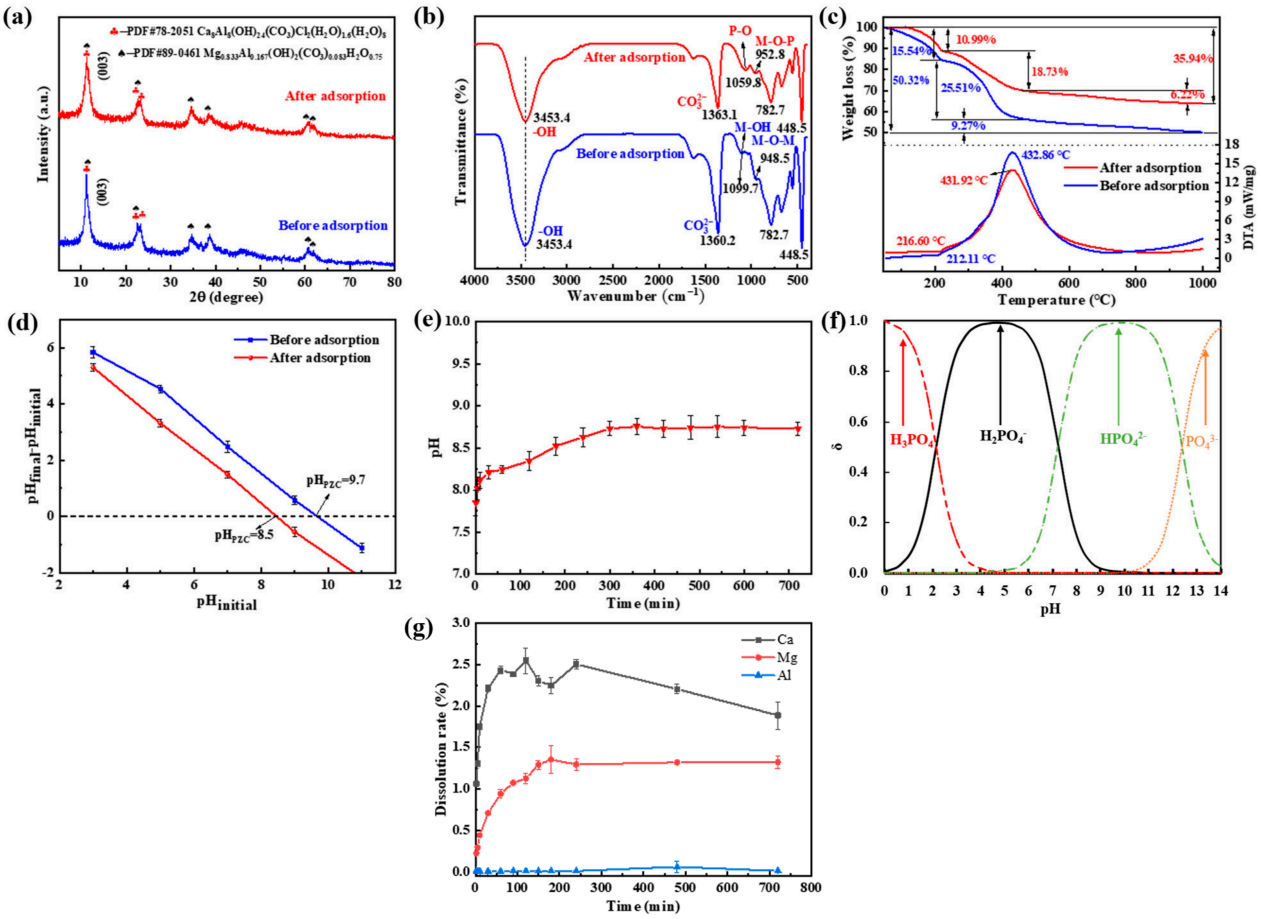


Figure 9. (**a**) XRD patterns, (**b**) FTIR spectra, (**c**) TG-DTA profiles, and (**d**) pH_{PZC} curves of LDHs before and after phosphate adsorption; (**e**) variation in solution pH, (**f**) phosphate species distribution as a function of pH during phosphate removal by Ca-Mg-Al LDHs; (**g**) temporal changes in the dissolution rates of major metal ions.

XPS analysis (Figure 10) provided further confirmation at the atomic level. The survey spectra (Figure 10a,b) showed the emergence of a P 2p signal with concomitant Cl 2p signal attenuation after adsorption, confirming phosphate immobilization with partial Cl^- displacement [39]. High-resolution spectra (Figure 10d–f) revealed positive binding energy shifts for Ca $2p_{3/2}$, Mg 1s, and Al 2p, reflecting decreased electron density at metal sites due to coordination with electron-withdrawing phosphate groups through M-O-P bonding [40,41]. The relatively pronounced Ca 2p shift further suggests Ca-O-P surface complex formation or amorphous Ca-P precipitation, consistent with the absence of crystalline Ca-P phases in XRD [42]. The Cl 2p spectrum (Figure 10g) showed negative binding energy shifts (Cl $2p_{3/2}$: 198.03 → 197.87 eV) with a marked reduction in Cl atomic content from 2.00% to 0.73%, providing direct evidence of anion exchange [43]. The P 2p spectrum (Figure 10h) exhibited a characteristic doublet at 133.24 eV (P $2p_{3/2}$) and 134.20 eV (P $2p_{1/2}$) exclusively in the post-adsorption sample, with binding energies indicative of chemically bonded phosphate rather than physisorbed species [37]. The C 1s spectrum remained unchanged before and after adsorption.

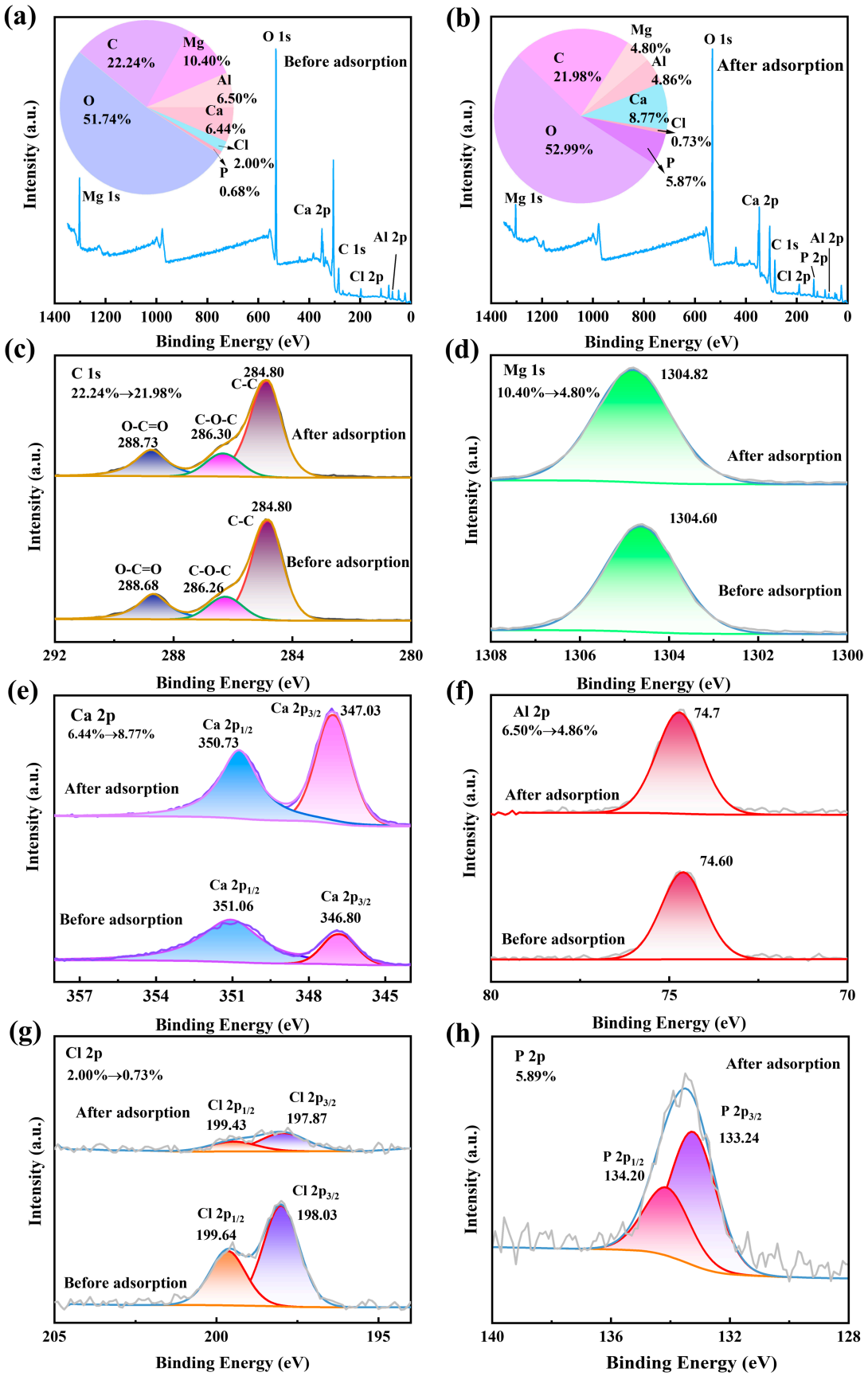


Figure 10. XPS analysis of Ca-Mg-Al LDHs before and after phosphate adsorption: (**a**,**b**) XPS survey spectra and surface elemental compositions before and after adsorption; high-resolution spectra of (**c**) C 1s, (**d**) Mg 1s, (**e**) Ca 2p, (**f**) Al 2p, (**g**) Cl 2p, and (**h**) P 2p.

The removal of phosphate by Ca-Mg-Al LDHs is governed by the interplay of several cooperative mechanisms. Based on the collective experimental evidence, the process can be resolved into four principal pathways. At the initial stage, electrostatic attraction drives HPO_4^{2-} toward the LDH surface. Because the working pH lies below the point of zero charge (pH_{PZC} = 9.70), the surface carries a net positive charge that promotes anion enrichment at the interface. Anion exchange within the interlayer region operates concurrently, though its contribution appears limited. XPS indicates that the Cl content drops from 2.00% to 0.73%, while FTIR shows weakened CO_3^{2-} bands and TG analysis records reduced weight loss in the high-temperature stage. These changes point to partial displacement of interlayer Cl^- and CO_3^{2-} by HPO_4^{2-}. Yet the absence of interlayer expansion in the XRD patterns suggests that this pathway remains supplementary rather than dominant. The most substantial removal proceeds through surface ligand exchange. HPO_4^{2-} displaces coordinated surface hydroxyl groups to form inner-sphere M-O-P complexes. This interpretation is consistent with the appearance of new FTIR bands at 1059.80 and 952.80 cm^{-1}, positive binding energy shifts for the structural metals in XPS, and a P 2p profile characteristic of chemisorbed phosphate. In addition, the rise in solution pH indicates OH^- release during ligand exchange, whereas the lowered pH_{PZC} points to enhanced surface negativity as phosphate binds to the metal centers. A fourth pathway involves Ca^{2+} released from limited surface dissolution (<4 mg/L). This calcium reacts with HPO_4^{2-} to precipitate amorphous calcium phosphate phases on the LDH surface. The pronounced shift in the Ca 2p peak and the absence of crystalline Ca-P reflections in XRD support this interpretation. Overall, surface ligand exchange functions as the dominant mechanism. The presence of Ca^{2+} introduces a precipitation pathway that conventional Mg-Al LDHs lack, and the synergy between chemisorption and precipitation accounts for the high removal capacity and the effective, essentially irreversible immobilization of phosphate.

3.4. Comparison with Other Literature

As shown in Table 7, the phosphate adsorption capacity of the synthesized Ca-Mg-Al-Cl/CO_3 LDHs is comparable to that of several reported Ca-Mg-Al and Mg-Fe LDHs. Although some modified LDHs exhibit higher adsorption capacities, these materials are typically synthesized from high-purity chemical reagents and often require additional modification or functionalization procedures. In contrast, the present adsorbent was prepared using phosphate tailings as the primary source of Ca and Mg, providing a low-cost and sustainable route for LDH synthesis while simultaneously promoting phosphate tailings valorization. Therefore, this study provides a feasible strategy for integrating phosphate tailings utilization with phosphate removal from wastewater, contributing to both sustainable resource use and environmental remediation.

Table 7. Comparison of phosphate adsorption capacities of the synthesized Ca-Mg-Al LDHs with representative phosphate adsorbents reported in the recent literature.

Adsorbents	Adsorption Conditions	Initial P Concentration (mg/L)	q_m (mg/g)	References
Ca-Al-CO_3 LDHs	pH = 6, t = 90 min, T = 30 °C	40	77.29	[41]
Ca-Al-CO_3-Asp LDHs	pH = 6, t = 120 min, T = 30 °C	40	185.98	[41]
Ca-Al-Cl LDHs	pH = 7, t = 24 h, T = 25 °C	200	125.00	[44]
Mg-Al-Cl LDHs	pH = 5, t = 300 min, T = 25 °C	500	69.75	[45]
Mg-Al-Cl/CO_3 LDHs	pH = 5.6, t = 5–60 min, T = 25 °C	50	60–70	[40]
Ca-Mg-Al-Cl LDHs	pH = 8, T = 25 °C	50	21.48	[46]
Ca-Mg-Al LDOs	pH = 4, t = 200~500 min, T = 25 °C	33	40.66	[47]
Mg-Fe-Cl LDHs	pH = 7.0, t = 20 h, T = 20~25°C	10	9.80	[6]
Ca-Mg-Al-Cl/CO_3 LDHs	pH = 7.9, t = 150 min, T = 20–25 °C	50	38.61	This work

4. Conclusions

In this study, calcareous–magnesian PTs were used as raw materials to prepare Ca-Mg-Al LDHs through selective hydrothermal leaching combined with co-precipitation, and the resulting product was evaluated for phosphate adsorption from wastewater. The main conclusions are drawn as follows:

(1) Hydrothermal leaching with $AlCl_3$ solution selectively decomposed the dolomite phase in the PTs. The leaching rates of Ca and Mg reached 77.87% and 99.69%, respectively, whereas only 7.53% of P was dissolved. The obtained leachate could be used directly as the precursor solution for LDH synthesis.

(2) The synthesis pH was the determining factor for Ca incorporation into the LDH layer structure. Under the conditions of pH 12, aging at 40 °C for 2 h, the prepared Ca-Mg-Al LDHs possessed good crystallinity, well-defined platelet morphology, and homogeneous elemental distribution.

(3) The Ca-Mg-Al LDHs exhibited a maximum phosphate adsorption capacity of 38.61 mg-P/g as fitted by the Langmuir model. The adsorption kinetics obeyed the pseudo-second-order model, and intraparticle diffusion analysis indicated that the process was governed by multiple mass-transfer steps.

(4) Mechanistic investigation revealed that phosphate removal was dominated by surface ligand exchange, leading to M-O-P inner-sphere complexes, supplemented by interlayer anion exchange, electrostatic attraction, and amorphous Ca-P surface precipitation. The incorporation of Ca into the ternary LDH system introduced a precipitation pathway that is unavailable in conventional Mg-Al LDHs, facilitating the irreversible immobilization of phosphate.

Author Contributions: Methodology, Writing—original draft, Data curation, Writing—review and editing, Z.W.; Software, Data curation, Writing—original draft, H.J.; Visualization, Investigation, Data curation. Software, B.L.; Conceptualization, Writing—review and editing, Y.Z.; Visualization, Writing-review and editing, J.L.; Conceptualization, Supervision, Funding acquisition, Project administration, Writing—review and editing, C.H. All authors have read and agreed to the published version of the manuscript.

Funding: This research was funded by the Open Fund Project of the National Engineering Research Center for Phosphate Resources Development and Utilization (NECP2025-07).

Data Availability Statement: The raw data supporting the conclusions of this study are available from the authors upon reasonable request.

Conflicts of Interest: The authors declare no conflicts of interest.

References

1. Everaert, M.; Warrinnier, R.; Baken, S.; Gustafsson, J.-P.; De Vos, D.; Smolders, E. Phosphate-Exchanged Mg–Al Layered Double Hydroxides: A New Slow Release Phosphate Fertilizer. *ACS Sustain. Chem. Eng.* **2016**, *4*, 4280–4287. [CrossRef]
2. Yin, H.; Zhang, M.; Yin, P.; Li, J. Characterization of internal phosphorus loading in the sediment of a large eutrophic lake (Lake Taihu, China). *Water Res.* **2022**, *225*, 119125. [CrossRef] [PubMed]
3. Gibbons, K.J.; Bridgeman, T.B. Effect of temperature on phosphorus flux from anoxic western Lake Erie sediments. *Water Res.* **2020**, *182*, 116022. [CrossRef] [PubMed]
4. Gong, H.; Wu, J.; Feng, G.; Jiao, X. Phosphorus supply chain for sustainable food production will have mitigated environmental pressure with region-specific phosphorus management. *Resour. Conserv. Recycl.* **2023**, *188*, 106686. [CrossRef]
5. Jin, X.; Guo, J.; Hossain, M.F.; Lu, J.; Lu, Q.; Zhou, Y.; Zhou, Y. Recent advances in the removal and recovery of phosphorus from aqueous solution by metal-based adsorbents: A review. *Resour. Conserv. Recycl.* **2024**, *204*, 107464. [CrossRef]
6. Bacelo, H.; Pintor, A.M.A.; Santos, S.C.R.; Boaventura, R.A.R.; Botelho, C.M.S. Performance and prospects of different adsorbents for phosphorus uptake and recovery from water. *Chem. Eng. J.* **2020**, *381*, 122566. [CrossRef]

7. Liu, Y.; Wang, S.; Huo, J.; Zhang, X.; Wen, H.; Zhang, D.; Zhao, Y.; Kang, D.; Guo, W.; Ngo, H.H. Adsorption recovery of phosphorus in contaminated water by calcium modified biochar derived from spent coffee grounds. *Sci. Total Environ.* **2023**, *909*, 168426. [CrossRef] [PubMed]
8. Li, X.; Shu, J.; Zhao, H.; Wang, J.; Chen, M.; Li, B. A Critical Review on Approaches for Phosphorus Ore Flotation Tailings Treatment and Disposal Technology: Environment Properties, Comprehensive Utilization, and Resource Utilization. *Ind. Eng. Chem. Res.* **2024**, *63*, 1191–1199. [CrossRef]
9. Boumaza, B.; Kechiched, R.; Chekushina, T.V.; Benabdeslam, N.; Senouci, K.; Hamitouche, A.Y.-E.; Merzeg, F.A.; Rezgui, W.; Rebouh, N.Y.; Harizi, K. Geochemical distribution and environmental assessment of potentially toxic elements in farmland soils, sediments, and tailings from phosphate industrial area (NE Algeria). *J. Hazard. Mater.* **2023**, *465*, 133110. [CrossRef] [PubMed]
10. Moukannaa, S.; Loutou, M.; Benzaazoua, M.; Vitola, L.; Alami, J.; Hakkou, R. Recycling of phosphate mine tailings for the production of geopolymers. *J. Clean. Prod.* **2018**, *185*, 891–903. [CrossRef]
11. Jun, J.D.; Huang, X.; Liang, L.; Huang, L. Research hotspot and trend of resource utilization of phosphorus tailings—Based on Citespace and VOSviewer visualization. *Physicochem. Probl. Miner. Process.* **2024**, *60*, 192132. [CrossRef]
12. Yu, Y.-H.; Du, C.-M. Leaching of phosphorus from phosphate tailings and extraction of calcium phosphates: Toward comprehensive utilization of tailing resources. *J. Environ. Manag.* **2023**, *347*, 119159. [CrossRef] [PubMed]
13. Jin, C.; Chen, B.; Qu, G.; Qin, J.; Yang, J.; Liu, Y.; Li, H.; Wu, F.; He, M. $NaHCO_3$ synergistic electrokinetics extraction of F, P, and Mn from phosphate ore flotation tailings. *J. Water Process Eng.* **2023**, *54*, 104013. [CrossRef]
14. Wang, Q.; O'Hare, D. Recent Advances in the Synthesis and Application of Layered Double Hydroxide (LDH) Nanosheets. *Chem. Rev.* **2012**, *112*, 4124–4155. [CrossRef] [PubMed]
15. Fan, G.; Li, F.; Evans, D.G.; Duan, X. Catalytic applications of layered double hydroxides: Recent advances and perspectives. *Chem. Soc. Rev.* **2014**, *43*, 7040–7066. [CrossRef] [PubMed]
16. Xu, M.; Wei, M. Layered Double Hydroxide-Based Catalysts: Recent Advances in Preparation, Structure, and Applications. *Adv. Funct. Mater.* **2018**, *28*, 1802943. [CrossRef]
17. Goh, K.-H.; Lim, T.-T.; Dong, Z. Application of layered double hydroxides for removal of oxyanions: A review. *Water Res.* **2008**, *42*, 1343–1368. [CrossRef] [PubMed]
18. Yu, Y.-H.; Du, C.-M.; Zhang, Y.-T.; Yuan, R.-Y. Phosphorus recovery from phosphate tailings through a two-stage leaching-precipitation process: Toward the harmless and reduction treatment of P-bearing wastes. *Environ. Res.* **2024**, *248*, 118328. [CrossRef] [PubMed]
19. Zheng, Y.; Wan, Y.; Zhang, Y.; Huang, J.; Yang, Y.; Tsang, D.; Wang, H.; Chen, H.; Gao, B. Recovery of phosphorus from wastewater: A review based on current phosphorous removal technologies. *Crit. Rev. Environ. Sci. Technol.* **2023**, *53*, 1148–1172. [CrossRef] [PubMed]
20. Alidokht, L.; Oustan, S.; Khataee, A.; Neyshabouri, M.; Reyhanitabar, A. Removal of chromate from aqueous solution by reduction with nanoscale Fe-Al layered double hydroxide. *Res. Chem. Intermed.* **2018**, *44*, 2319–2331. [CrossRef]
21. Abderrazek, K.; Srasra, N.; Srasra, E. Synthesis and Characterization of Zn-Al Layered Double Hydroxides: Effect of the Operating Parameters. *J. Chin. Chem. Soc.* **2017**, *64*, 346–353. [CrossRef]
22. Sen Gupta, S.; Bhattacharyya, K.G. Kinetics of adsorption of metal ions on inorganic materials: A review. *Adv. Colloid Interface Sci.* **2011**, *162*, 39–58. [CrossRef] [PubMed]
23. Langmuir, I. The adsorption of gases on plane surfaces of glass, mica and platinum. *J. Am. Chem. Soc.* **1918**, *40*, 1361–1403. [CrossRef]
24. Chung, H.-K.; Kim, W.-H.; Park, J.; Cho, J.; Jeong, T.-Y.; Park, P.-K. Application of Langmuir and Freundlich isotherms to predict adsorbate removal efficiency or required amount of adsorbent. *J. Ind. Eng. Chem.* **2015**, *28*, 241–246. [CrossRef]
25. Buates, J.; Imai, T. Biochar functionalization with layered double hydroxides composites: Preparation, characterization, and application for effective phosphate removal. *J. Water Process Eng.* **2020**, *37*, 101508. [CrossRef]
26. Seftel, E.M.; Ciocarlan, R.G.; Michielsen, B.; Meynen, V.; Mullens, S.; Cool, P. Insights into phosphate adsorption behavior on structurally modified ZnAl layered double hydroxides. *Appl. Clay Sci.* **2018**, *165*, 234–246. [CrossRef]
27. Ho, Y.S. Review of second-order models for adsorption systems. *J. Hazard. Mater.* **2006**, *136*, 681–689. [CrossRef] [PubMed]
28. Simonin, J.-P. On the comparison of pseudo-first order and pseudo-second order rate laws in the modeling of adsorption kinetics. *Chem. Eng. J.* **2016**, *300*, 254–263. [CrossRef]
29. Ho, Y.; McKay, G. Pseudo-second order model for sorption processes. *Process Biochem.* **1999**, *34*, 451–465. [CrossRef]
30. Weber Walter, J.; Morris, J.C. Kinetics of Adsorption on Carbon from Solution. *J. Sanit. Eng. Div.* **1963**, *89*, 31–59. [CrossRef]
31. Qing, Z.; Qin, Q.; Wang, L.; Jiang, C.; Yang, Z.; Liu, Y.; Zhang, S.; Chen, J. Rapid and efficient removal of phosphate by La-doped layered double hydroxide/biochar from aqueous solution. *New J. Chem.* **2024**, *48*, 3208–3220. [CrossRef]
32. Bezza, F.A.; Brink, H.G.; Chirwa, E.M.N. Selective and efficient removal of phosphate from aqueous solution using activated carbon-supported Mg–Fe layered double oxide nanocomposites. *Can. J. Chem. Eng.* **2024**, *103*, 524–542. [CrossRef]

33. Jiang, S.; Yu, T.; Xia, R.; Wang, X.; Gao, M. Realization of super high adsorption capability of 2D δ-MnO_2/GO through intra-particle diffusion. *Mater. Chem. Phys.* **2019**, *232*, 374–381. [CrossRef]
34. Novillo, C.; Guaya, D.; Allen-Perkins Avendaño, A.; Armijos, C.; Cortina, J.L.; Cota, I. Evaluation of phosphate removal capacity of Mg/Al layered double hydroxides from aqueous solutions. *Fuel* **2014**, *138*, 72–79. [CrossRef]
35. Kim, T.-H.; Lundehøj, L.; Nielsen, U.G. An investigation of the phosphate removal mechanism by MgFe layered double hydroxides. *Appl. Clay Sci.* **2020**, *189*, 105521. [CrossRef]
36. Liu, C.; Zhang, M.; Pan, G.; Lundehøj, L.; Nielsen, U.G.; Shi, Y.; Hansen, H.C.B. Phosphate capture by ultrathin MgAl layered double hydroxide nanoparticles. *Appl. Clay Sci.* **2019**, *177*, 82–90. [CrossRef]
37. Dox, K.; Everaert, M.; Merckx, R.; Smolders, E. Optimization of phosphate recovery from urine by layered double hydroxides. *Sci. Total Environ.* **2019**, *682*, 437–446. [CrossRef] [PubMed]
38. Pan, Y.; Li, L.; Lu, K.; Hong, X.; Gao, J.; Xia, M.; Wang, F. Synergistic adsorption of real phosphorus-containing domestic wastewater by in-situ growth of MgFe-layered double hydroxides co-doped with dual-functional lignosulfonate and $La(OH)_3$ on wood-derived cellulose aerogel. *Chem. Eng. J.* **2024**, *493*, 152725. [CrossRef]
39. Guo, Q.; Yin, C.; Chen, Y.; Fang, Z.; Xiao, H.; He, J.; Huang, L.; Wu, G.; Zeng, Z.; Shen, F.; et al. Periodic pH regulation controls the phosphate uptake-release behavior and structural evolution of layered double hydroxides. *Chem. Eng. J.* **2023**, *459*, 141584. [CrossRef]
40. Tong, Q.; Cheng, P.; Jiang, G.; Li, Y.; Wei, Y.; Zou, Y.; Lv, X.; Ao, L. Hierarchical flower-like MgAl layered double hydroxide microparticles as phosphate porter for its recovery from phosphate-contaminated water. *Sep. Purif. Technol.* **2024**, *330*, 125384. [CrossRef]
41. Zeng, Z.; Zheng, J.; Li, X.; Fan, C.; Zeng, R.; Tang, W. Phosphate adsorption by amino acids intercalated calcium aluminum hydrotalcites: Kinetic, isothermal and mechanistic studies. *J. Solid State Chem.* **2024**, *329*, 124428. [CrossRef]
42. Dan, L.; Nan, H.; Zhang, Y.; Sher, F.; Wang, C. Phosphorus recovery from wastewater by Ca-Al layered double hydroxide/biochar as potential agricultural phosphorus for closed-loop phosphorus recycling. *Process Saf. Environ. Prot.* **2025**, *194*, 1538–1548. [CrossRef]
43. Fang, D.; Huang, L.; Fan, J.; Xiao, H.; Wu, G.; Wang, Y.; Zeng, Z.; Shen, F.; Deng, S.; Ji, F. New insights into the arrangement pattern of layered double hydroxide nanosheets and their ion-exchange behavior with phosphate. *Chem. Eng. J.* **2022**, *441*, 136057. [CrossRef]
44. Qiu, S.; Zhao, D.; Feng, Y.; Li, M.; Liang, X.; Zhang, L.; Luo, Y.; Zhang, K.; Wang, F. Adsorption performance and mechanism of Ca-Al-LDHs prepared by oyster shell and pop can for phosphate from aqueous solutions. *J. Environ. Manag.* **2022**, *303*, 114235. [CrossRef] [PubMed]
45. Luengo, C.V.; Volpe, M.A.; Avena, M.J. High sorption of phosphate on Mg-Al layered double hydroxides: Kinetics and equilibrium. *J. Environ. Chem. Eng.* **2017**, *5*, 4656–4662. [CrossRef]
46. Jurado-Davila, V.; Schneider, I.A.H.; Féris, L.A. Synthesis of Ca-Mg-Al layered double hydroxide from dolomite with ultrasound-assisted method. Application in phosphate removal. *Inorg. Chem. Commun.* **2024**, *159*, 111829. [CrossRef]
47. Xiao, L.; Wang, Z.; Wang, D.; Lan, Y.; Kong, Q. Preparation of CaMgAl-calcined layered double hydroxides and application on the removal of phosphates. *Water Sci. Technol.* **2023**, *87*, 798–811. [CrossRef] [PubMed]

Disclaimer/Publisher's Note: The statements, opinions and data contained in all publications are solely those of the individual author(s) and contributor(s) and not of MDPI and/or the editor(s). MDPI and/or the editor(s) disclaim responsibility for any injury to people or property resulting from any ideas, methods, instructions or products referred to in the content.